Modification of a Broadband Engine Noise Simulator for Enhanced Aft Fan Noise Representation

Kelly M. Shelts*, Ian A. Clark†, and Yueping Guo‡
NASA Langley Research Center, Hampton, VA, 23681

Modifications to an existing broadband noise source (BNS) model were tested in the anechoic chamber of the Structural Acoustics Loads and Transmission (SALT) facility at the NASA Langley Research Center with the goal of simulating the aft fan broadband noise produced by a high-bypass ratio turbofan engine. High geometric-resolution acoustic measurements, spanning a hemisphere in the acoustic far field, were acquired using the High Resolution Traversing Microphone Array (HiRTMA). Modifications included additively manufactured waveguides that attached to the existing BNS hardware to create a converging-diverging channel around a new plug to guide sound waves towards the desired peak radiation direction. An investigation was also performed of the isolated impinging air jet noise sources housed in the BNS to better understand the noise generation mechanisms. The optimum BNS configuration preserved the acoustic directivity observed for the isolated impinging jet and showed good agreement to published models for aft fan broadband noise.

I. Introduction

Aircraft noise continues to be a problem for communities near airports and commercial flight paths. The high levels of noise produced, particularly during takeoff and landing, can cause annoyance as well as negative stress-related health effects like sleep disruption and cardiovascular disorders [1]. Previous studies have found that interactions between an aircraft's engine and airframe are a large contributor to total aircraft system noise, especially for unconventional aircraft configurations [2, 3]. These interaction effects must be understood to enable higher fidelity predictions and contribute to the development of low-noise aircraft. While flow effects are important, valuable studies of acoustic scattering effects, like reflection and shielding, can be conducted in a static anechoic environment. In order to set up a representative experiment that captures the dominant effects of engine noise scattering around an airframe, a noise simulator is required with similar acoustic characteristics to the particular engine source under consideration. As industry moves towards higher-bypass ratio turbofan engines, broadband fan noise has been shown to be a major component of total engine noise [4]. This work seeks to produce a noise simulator that has the representative characteristics of aft-radiated broadband fan noise.

A successful noise simulator should maintain geometric similarity to a real aircraft engine, generate high sound levels, produce appropriate spectral content, and exhibit representative noise directivity. Previous studies show that full-scale aft broadband fan noise is dominant between 1 and 5 kHz with peak noise amplitude near 3 kHz at an angle approximately 140° from the engine's axial centerline [5, 6]. For future studies, an 8-12% scale airframe is planned, so the simulator should have high noise levels and the desired directivity between approximately 8 and 50 kHz.

The Broadband Noise Simulator (BNS) is a hardware system previously used in wind tunnel acoustic experiments to study engine placement effects on shielding of exhaust broadband noise radiation [7]. The BNS was previously known as the Broadband Engine Noise Simulator (BENS) but is referred to here as the BNS to focus on specific engine noise components rather than total broadband engine noise. The BNS is a model nacelle housing three impinging jet devices using compressed air to generate broadband noise; more detail is available in Brehm, et.al [8]. Preliminary testing determined this source generates appropriate noise levels and spectral content, but most of the noise is directed in line with the exhaust. In this study, modifications to the existing BNS hardware are designed and tested with the goal of altering its noise directivity to be more representative of aft fan noise.

These modifications can be studied in a static anechoic environment, which provides a controlled setting in which to isolate variables and efficiently iterate between configurations. The experiments were done in the anechoic portion of the Structural Acoustics Loads and Transmission Facility (SALT) [9], using the High Resolution Traversing Microphone

*Research Aerospace Engineer, Aeroacoustics Branch, AIAA Member, kelly.m.shelts@nasa.gov.
†Research Aerospace Engineer, Aeroacoustics Branch, AIAA Senior Member
‡Senior Research Engineer, Aeroacoustics Branch, AIAA Associate Fellow

Array (HiRTMA) [10]. This paper describes the modifications tested, experimental procedures, and compares results to existing models of aft broadband fan noise.

II. Experimental Methods

The following section outlines the experimental methods employed in this study. It includes detailed descriptions of the test hardware, measurement system, facility setup, and procedures used to acquire and process acoustic data. These methods were selected to enable precise evaluation of the noise source and its modifications.

A. SALT

The SALT facility at the NASA Langley Research Center is a state-of-the-art reverberant-anechoic test suite designed for a wide range of acoustic experiments. For this study, the experiment was conducted in the anechoic chamber of the facility, which measures 25 x 30 x 17 feet. The chamber was specifically designed to minimize reflections, with the floor, ceiling, and walls treated with three-foot-tall, open-cell, polyurethane foam wedges, ensuring an environment that simulates free-field radiation conditions for frequencies above 80 Hz [9]. This setup provided an ideal testing environment to accurately measure acoustic phenomena without interference from unwanted reflections, allowing for precise analysis of noise sources and directivity patterns.

B. HiRTMA

Measurements were acquired using the High Resolution Traversing Microphone Array (HiRTMA), a precision acoustic measurement system designed to capture hemispherical sound fields around noise sources. HiRTMA consists of a suspended 14-foot diameter arc that supports 31 microphones evenly spaced along its length, each located six feet from the geometric center of the arc, as illustrated in Figure 1. The arc was mounted on a motorized rotation stage that enables full 360° rotation about the test article, allowing for high-resolution sampling of the acoustic field over an entire hemisphere. Microphones were positioned at 6° intervals along the arc, with alternating offsets on either side to achieve an effective angular resolution of 3° when combined with a full ±180° rotation, as shown in Figure 2. This dense spatial resolution supported accurate characterization of directivity patterns and scattering effects. For the present study, the arc was rotated in 10° increments, resulting in the measurement grid shown in Figure 3.

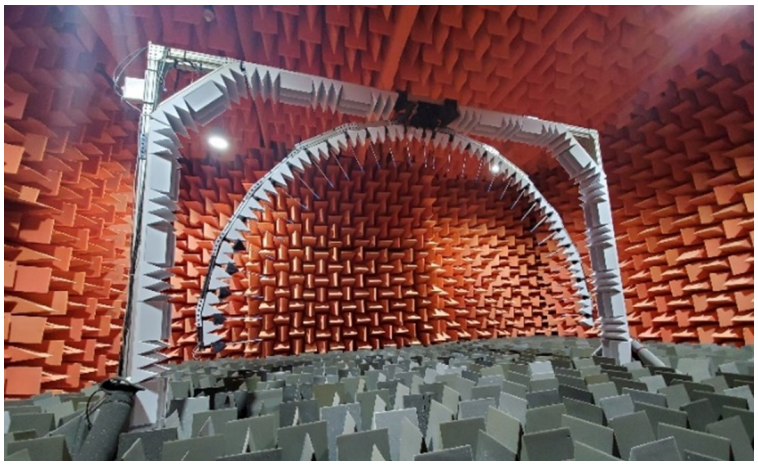

Fig. 1 High Resolution Traversing Microphone Array in Structural Acoustics Loads and Transmission Facility.

HiRTMA's acoustic performance was previously evaluated and validated in a dedicated experiment [10], confirming its suitability for precise far-field acoustic measurements. A previous study confirmed the acoustic far-field distance for the BNS by testing microphone positions at varying distances and verifying inverse-square law compliance. To minimize electromagnetic contamination from the motor controller during data acquisition, the rotation stage was fully disabled during each measurement. Transitions between positions were executed using a slow ramp-up/ramp-down motion profile to reduce mechanical vibrations and ensure repeatable, low-noise operation. The rotation system was driven by a precision motor and rotation stage, which enabled reliable positioning throughout the test campaign.

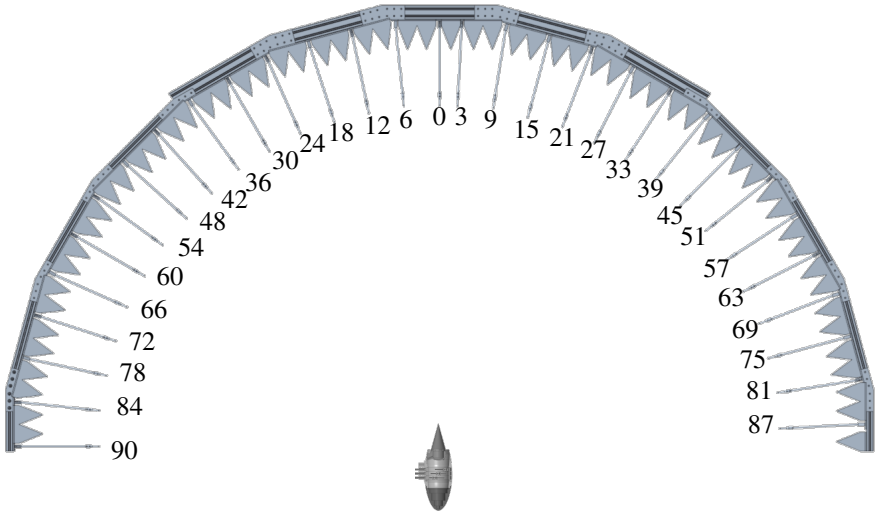

Fig. 2 BNS orientation with respect to HiRTMA arc, with polar angles of microphones (in degrees) illustrating the microphone offset enabling a 3° polar angle resolution with full rotation of the array.

C. Coordinate System

The measurement locations are shown in Figure 3, projected onto a flat plane for clarity. Each position is defined in spherical coordinates based on the HiRTMA geometry: the polar angle corresponds to the fixed microphone position along the HiRTMA arc and the azimuthal angle corresponds to the rotation angle of the arc about the test article, controlled by the motorized stage. This configuration allows for high-resolution, hemispherical sampling of the acoustic field around the source. For all tests in this paper, the source was positioned at the geometric center of the HiRTMA arc, with the source exhaust plane in line with the lowest microphone on the HiRTMA arc, as illustrated in Figure 2. The exhaust axis aligns with the 0° polar angle and the sideline microphone aligns with the 90° polar angle. This standard setup ensures consistent interpretation of directivity patterns and supports comparison across test configurations.

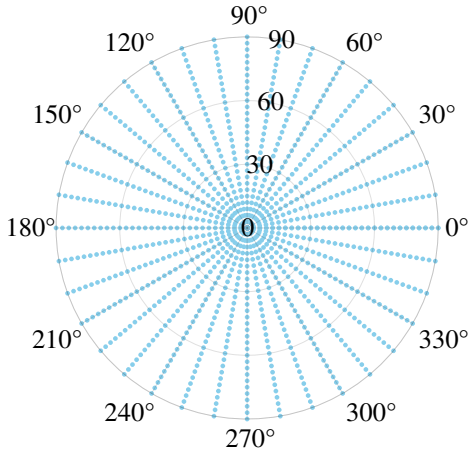

Fig. 3 HiRTMA measurement locations projected onto a flat plane. Polar angle varies from 0° to 90° radially, corresponding to microphone position along the physical arc. Azimuthal angle varies from 0° to 360° circumferentially, corresponding to rotation of the arc around its center.

D. Data Acquisition

HiRTMA was equipped with 31 ¼-inch free-field microphones with a frequency response range of 16 Hz to 80 kHz. For each position, data were acquired at a rate of 204,800 samples per second for 10 seconds. The frequency spectrum was calculated using Welch's method with a spectral bin width of 32 Hz and a Hanning window with a 50% overlap between time-history segments. Atmospheric corrections were applied using in-chamber temperature, pressure, and humidity readings. Pistonphone calibrations at 250 Hz were used to determine the individual microphone sensitivities for converting the outputs from volts to pascals. Electrostatic pressure responses, relative to the 250 Hz sensitivity, were subsequently used to apply dB corrections for frequencies between 20 Hz and 80 kHz.

E. BNS

The BNS nacelle consists of an open interior center section that houses up to three impinging jet devices, referred to as noise rings, as depicted in Figure 4a. The central section of the nacelle is approximately nine inches long with an internal diameter of about 6 inches, providing a compact and acoustically rigid housing for the noise sources. The inlet cover features a stepped internal surface to encourage acoustic scattering within the nacelle to create a diffuse sound field. The removable components of the BNS, shown in blue in Figure 4a, include the plug, aft nacelle section, and inlet cap, all of which can be interchanged or modified for different experimental configurations. The three internal mounting locations for the noise rings connect to individual plenums where pressurized air is connected. Each impinging jet source is composed of four coplanar jets with an internal diameter of 0.08 inches arranged in a cross pattern and directed at a central impingement point within the ring. These noise rings are modular and can be installed in any of the three axial plenum positions, or replaced with plain rings that contain no jets.

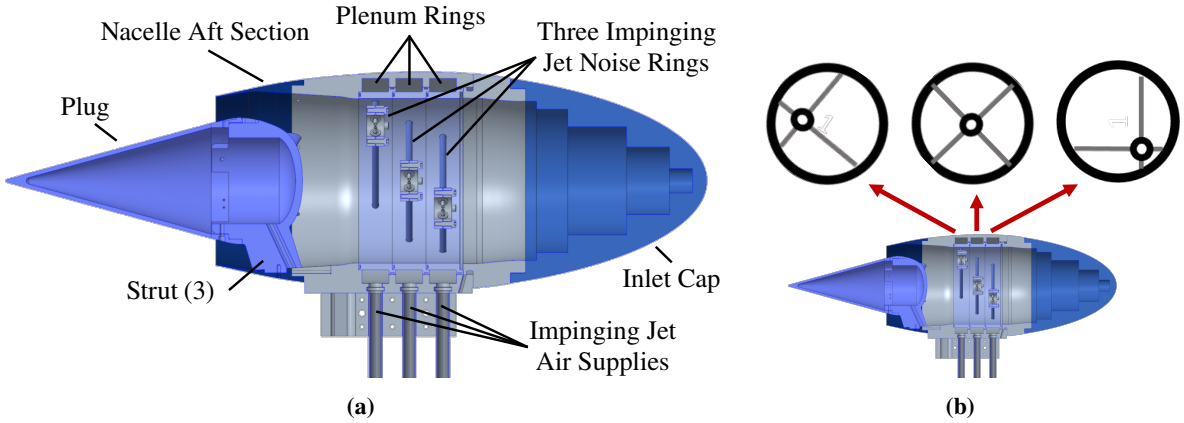

Fig. 4 Cross-section view of Broadband Noise Simulator BNS (a) and original BNS noise ring orientation, looking upstream (b)

The original BNS noise ring configuration is presented in Figure 4b, with three different impinging jet locations. For the waveguide orientations shown in this paper, one centered noise ring was installed in the most upstream position and plain rings with no impinging jets were installed in the two downstream slots. The optimized BNS configuration used a centered noise ring in the most downstream position, with plain rings installed in the upstream positions. In all tests, compressed air was supplied to each active plenum at 70 psia via 0.5-inch air lines.

F. Waveguides

The first attempts at changing the source directivity while maintaining geometric realism involved a series of 3D-printed exhaust modifications, referred to as waveguides. These waveguides replaced the nacelle aft section and plug and created a converging-diverging channel around a new plug. This was intended to guide sound waves towards the desired peak radiation direction. This was based in an assumption that the impinging jets were acting as omnidirectional point sources and a diffuse sound field was created within the BNS nacelle, which is discussed further in following sections. Multiple variations were tested, as illustrated in Figure 5, with differing parameters including strut configurations, curvature sharpness, plug diameter, and attachment mechanisms.

The first two waveguides, as shown in Figure 5, feature the same internal curvature, with exit channels angled 40° off

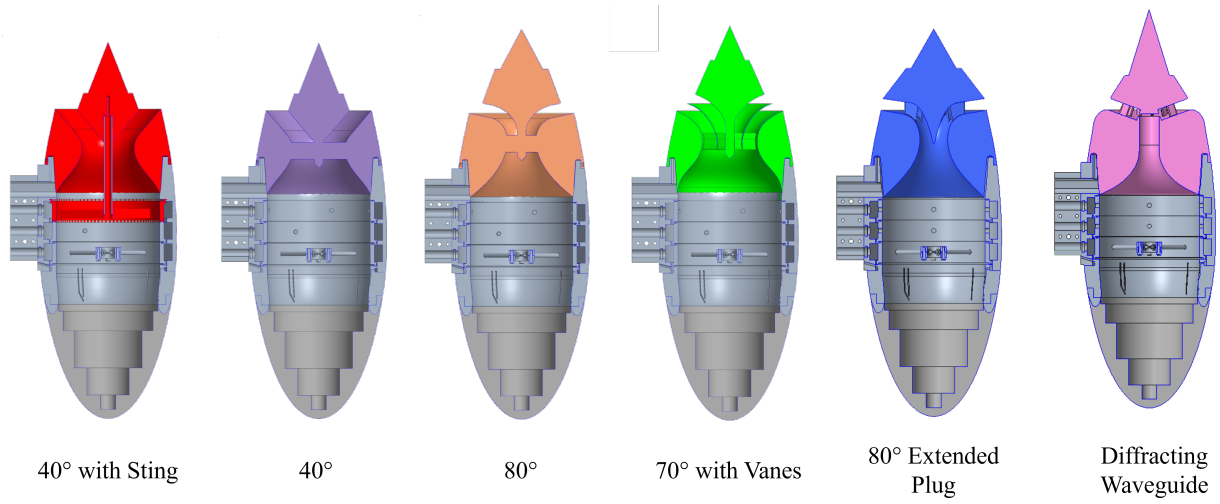

Fig. 5 Cross-section of waveguide designs.

the nacelle centerline. Both waveguides converge into a 2.4-inch-long straight section at the outlet, where the channel walls are parallel. This straight section was designed to be approximately five wavelengths long at a frequency of 30 kHz, and the final channel width measures 1 inch. The key difference between the two waveguides lies in the plug attachment mechanism. The first waveguide uses a sting-style attachment, secured via a placeholder noise ring. This design choice moved the six support struts further upstream from the nacelle exit plane, but it increased the complexity of both design and installation. In contrast, the second waveguide is a one-piece, 3D-printed component, incorporating eight plug support struts positioned at the throat of the waveguide.

The 80° waveguide has a more aggressive converging and diverging profile, with the final channel directed 80° from the nacelle exit axis. The plug is supported by eight struts at the waveguide throat, and the channel's final width is 0.7 inches, followed by a straight section extending 1.4 inches. The 70° version with vanes differs by including a divider vane that starts with the 8 plug supports at the throat of the waveguide. The two exit channels are 0.6 inches wide and were designed to increase exit area while targeting higher-frequency sound waves with narrower channels. The 80° Extended Plug waveguide shares the same converging and diverging geometry as the 80° waveguide but features a wider plug section. This wider plug was intended to reduce direct propagation paths toward the 0° polar angle. The plug is supported by 12 struts positioned further downstream compared to the previous waveguides, while the exit channel width remains 0.7 inches and extends straight for 1.4 inches. The diffracting waveguide introduces a significantly different design, with a converging section that feeds into a narrow 0.2-inch slit leading into a 0.7-inch-wide exit channel. This configuration was intended to create a diffraction-based sound source at the start of the exit channel, encouraging greater sound propagation in the channel's direction.

G. Noise Ring Fixture

The noise ring fixture is a standalone hardware assembly that enables pressurization of a single noise ring outside of the BNS nacelle for acoustic evaluation. A noise ring can be installed into a plenum with equal air supply to all four jet inlets, as shown in Figure 6. This can be used to investigate an individual noise ring's behavior and sensitivities without interactions with the nacelle's internal geometry. For all cases presented in this paper, 70 psi source pressure was used.

When installed in the fixture, the noise ring creates noise in both directions. To limit noise to one direction, an acoustically treated inlet cover was used to block noise radiation from one side of the noise ring fixture. The cover consisted of a 3D-printed plastic shell and the inside was lined with a 1.5-inch-thick layer of open-cell polyurethane foam. The shell was designed to fit with the existing noise ring fixture hardware to explore the potential interaction effects, not to emulate actual aircraft nacelle geometry.

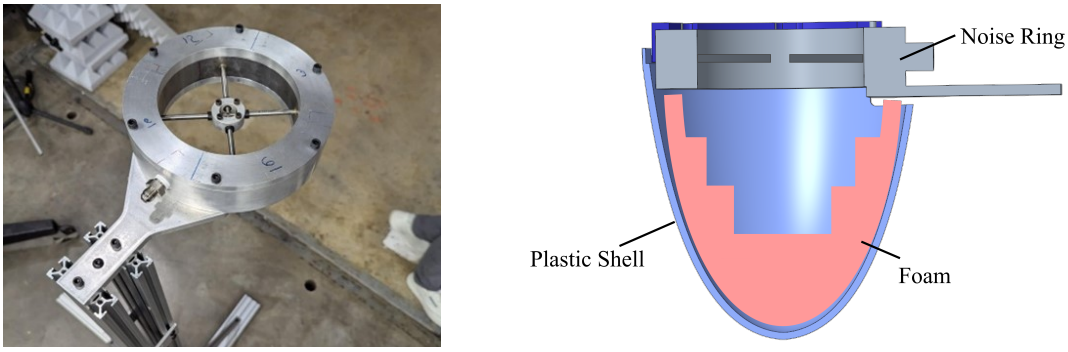

(a) (b)

Fig. 6 Noise ring installed in isolated fixture (a) and with acoustically lined inlet cover attachment (b).

H. Optimized BNS

Based on the results for the isolated noise ring, the BNS configuration was modified to preserve the isolated noise ring's characteristic behavior. The centered noise ring was installed in the most downstream position and all internal surfaces upstream of the noise ring were covered with a 1.5-inch-thick layer of open-cell polyurethane foam, as shown in Figure 7. The foam reduced reflections from the internal surfaces of the BNS, preventing a diffuse sound field from forming. The plug and nacelle aft section were removed to bring the noise ring closer to the exit of the nacelle model.

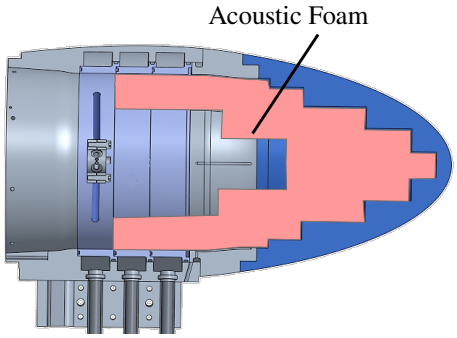

Fig. 7 Cross-section of Optimized BNS configuration.

III. Results and Discussion

This section presents comprehensive acoustic results for all configurations tested, focusing on spectra, directivity, and contour plots while providing an in-depth examination of the underlying physics and mechanisms responsible for the observed acoustic behavior. The analysis captures the iterative process involved in interpreting the data, detailing the challenges encountered and the insights gained. Results and discussion for the isolated noise ring configuration are presented first, although this configuration was tested after the original BNS and waveguide configurations during the experimental sequence. Unexpected results prompted additional investigation into the noise source itself, referred to as the isolated noise ring configuration. Presenting these findings first provides essential context for understanding the subsequent results. Second, results are presented from the original BNS and waveguide configurations, with physical explanation of measured results. Third, results from the optimized configurations are presented and compared with a fan noise prediction method developed by Krejsa and Stone to evaluate the performance of each configuration [5].

A. Isolated Noise Ring

In previous studies, an impinging jet noise source has been described as an omnidirectional broadband point source [11–13]. When this study began, it was assumed that each impinging jet inside the BNS was acting as an omnidirectional broadband point source. The waveguide results prompted additional investigation of the isolated noise ring, which

provided insight into the underlying noise-generating physics. The isolated noise ring fixture, shown in Figure 6, was installed in the center of the HiRTMA arc, with the impinging jets directly below the 0° microphone and in line with the 90° microphone. To observe source directivity, contour plots are created using all 1176 measurement locations shown in Figure 3. One-twelfth octave band averaged sound pressure levels are acquired for each measurement location and a polar contour plot is generated from these values. Each contour is normalized to the peak sound level and levels are presented as Δ dB to the maximum. Contours between 500 Hz and 60 kHz are presented in Figure 8. The impinging

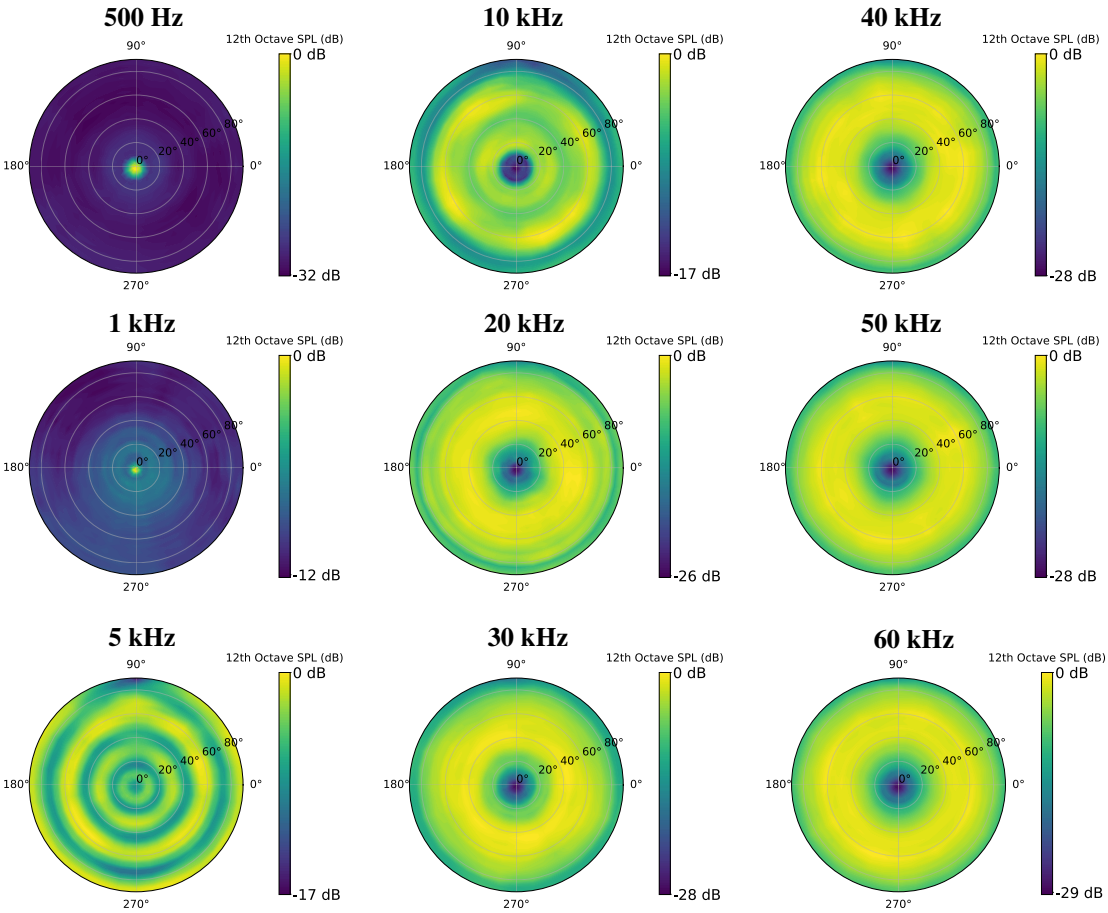

Fig. 8 One-twelfth-octave SPL contours of the isolated noise ring between 500 Hz and 60 kHz.

jets produce very frequency-dependent noise directivity. Below 1000 Hz, there is a strong peak directly above the impinging jets (at 0° polar angle). At 5 kHz, a strong interference pattern is observed. At this frequency, a wavelength is approximately the same length as the distance between the impinging jets and the internal surface of the noise ring. At frequencies above 10 kHz, the lowest sound levels are directly above the impinging jets, with peak sound levels around 40° polar angle. The overall trends in produced sound level and shifting directivity are shown in the spectogram of one-twelfth octave band SPL values from 100 Hz to 100 kHz in Figure 9. The mounting hardware for the isolated noise ring was located at the 90° azimuthal angle, causing slight axial asymmetry at that position, especially apparent in the 5 kHz contour plot. Besides that azimuthal angle, the levels were axisymmetric around the exhaust axis, with less than ±2 dB variation in one-twelfth octave sound pressure levels. Based on the measurements from the isolated noise ring (Figures 8 and 9), the following explanation of the noise-generating mechanisms is presented. The four jets impinge, and the resulting air stream is perpendicular to the jet directions, as shown in Figure 10. This was observed during testing, where the jet direction could be felt by a hand placed above the noise ring. The air stream carries low-frequency hydrodynamic pressure fluctuations, which are measured by the microphones as low-frequency excitation localized to the center of the jet stream, as seen in Figure 8 for 500 Hz and 1 kHz.

The high-frequency noise (above 10 kHz) is generated in the jet impingement region by turbulence and shock cell interactions, as described in [8]. The resulting jet—formed perpendicular to the four impinging jets—breaks up rapidly

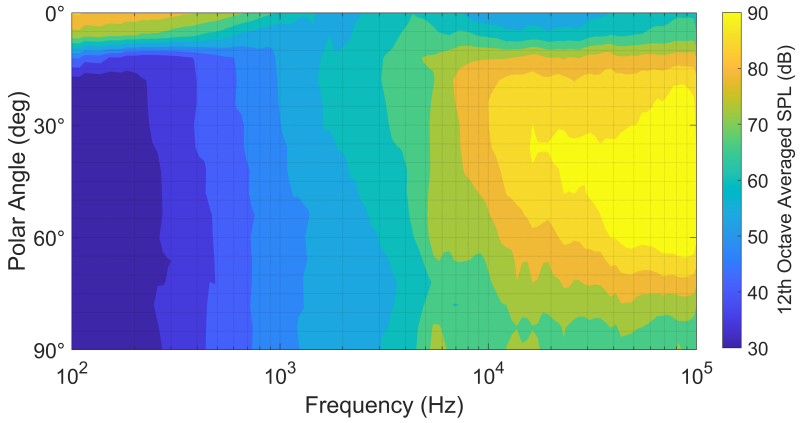

Fig. 9 One-twelfth-octave SPL spectogram of the isolated noise ring from 100 Hz to 100 kHz.

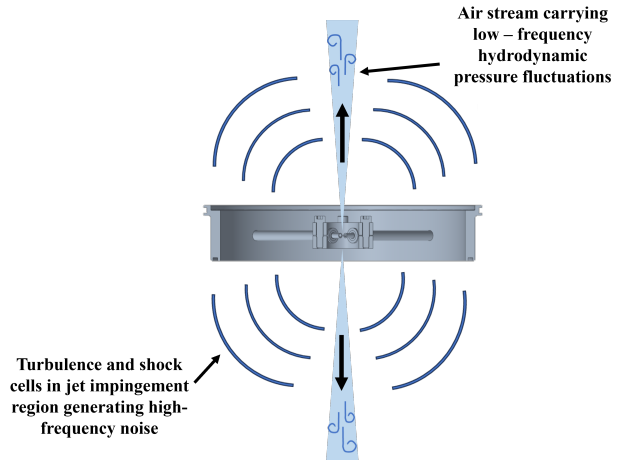

Fig. 10 Illustration of the impinging jet characteristics.

due to strong unsteadiness, with shock cells dissipating within approximately three nozzle diameters of the impingement zone. This confines the noise generation region to a relatively small area compared to the overall geometry of the noise ring. However, this noise is refracted by the air stream, which bends the propagation path away from the jet axis. As a result, the microphones measure very little noise directly along the centerline of the jet at high frequencies, resulting in peak noise at approximately 40° polar angle, as seen in Figure 8 for frequencies above 10 kHz. The significant SPL drop at the extreme microphone angles is presumably due to physical shielding of the sources by the plenum ring. The expanded measurement space and increased resolution of this test reveal that impinging jets do not radiate as simple omnidirectional, broadband point sources; rather, they have a more complex radiation pattern, as suggested in [8].

B. Original BNS and Waveguides

An understanding of the noise ring's aeroacoustic behavior clarifies the results from the original BNS configuration. For all measurements, the BNS was installed in the center of the HiRTMA arc, with its axial centerline aligned with the 0° microphone and the nozzle exit plane in line with the 90° microphone. With three noise rings, the BNS produces the highest noise levels in line with the exhaust axis, shown by the 0° line in Figure 11. These levels start to decrease significantly at 30° off axis and decay to approximately 15 dB below their peak levels at the sideline position, shown as the 90° line in Figure 11. The highest noise levels occur between 10 and 40 kHz for all microphone positions.

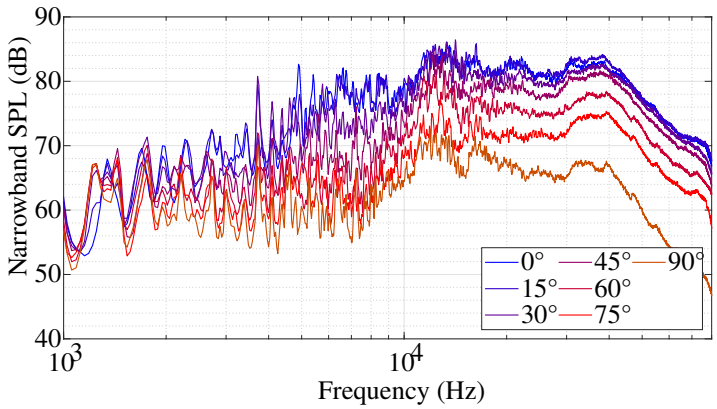

Fig. 11 Narrowband far-field acoustic spectra of baseline BNS configuration with 3 noise rings at 70 psi at multiple polar angles.

Contours centered around the 30 kHz one-twelfth octave band for four different configurations are presented in Figure 12. Figure 12a shows similar trends to Figure 11 for the baseline BNS configuration, with the highest noise levels in line with the exhaust axis of the nacelle. Due to the orientation of the noise rings inside the nacelle, there is some axial asymmetry in the center of the measurement field, but the sound levels are axisymmetric beyond 30 degrees polar angle, with less than ± 2 dB variation in one-twelfth octave band SPL levels for the original BNS configurations. Figure 12b shows the effects of a single source within the nacelle, with the same air supply pressure. The peak sound levels are lower, as observable in Figure 13, and the sound is more concentrated towards the exhaust axis, with levels dropping significantly beyond 15° polar angle. Figure 12c shows levels for a case with the 40° Sting waveguide with a single centered noise ring installed in the most upstream position of the BNS, as depicted in Figure 5. For this waveguide, the

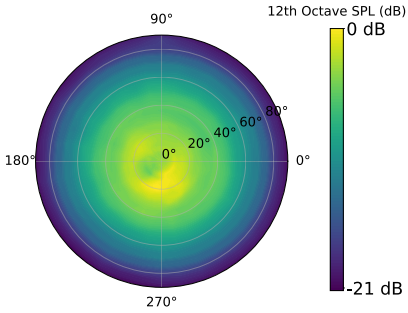

(a) Original BNS - three noise rings

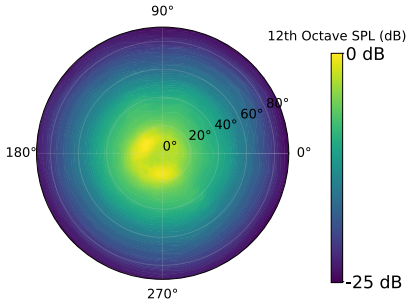

(b) Original BNS - one noise ring

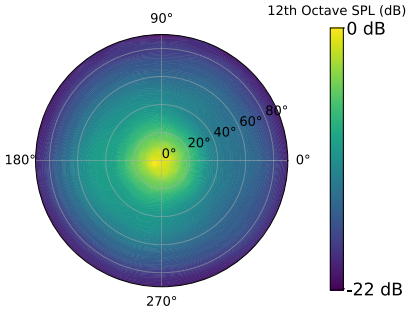

(c) 40° Sting Waveguide

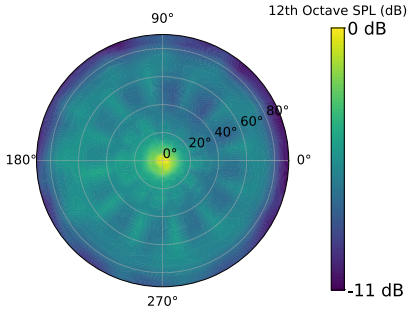

(d) 80° Extended Plug Waveguide

Fig. 12 30 kHz one-twelfth octave band SPL contours normalized to the contour peak level for the BNS in its original configuration (a,b), with the 40° sting waveguide (c), and with the 80° extended plug waveguide (d).

plug is supported by six struts at the plenum location. The highest noise levels again occur along the exhaust axis, but with sharper sound pressure level (SPL) rolloff towards the higher microphone angles than the single noise ring BNS case. Figure 12d shows levels for the 80° Extended Plug waveguide that has a plug supported by 12 struts near the exhaust outlet, which are observable in the contour plot as azimuthally spaced peaks. As for the previous configurations, the peak noise level is along the nacelle exhaust axis. Between 10° and 80° microphone angles, the sound levels are relatively constant compared to the other configurations but drop off between 80° and 90°.

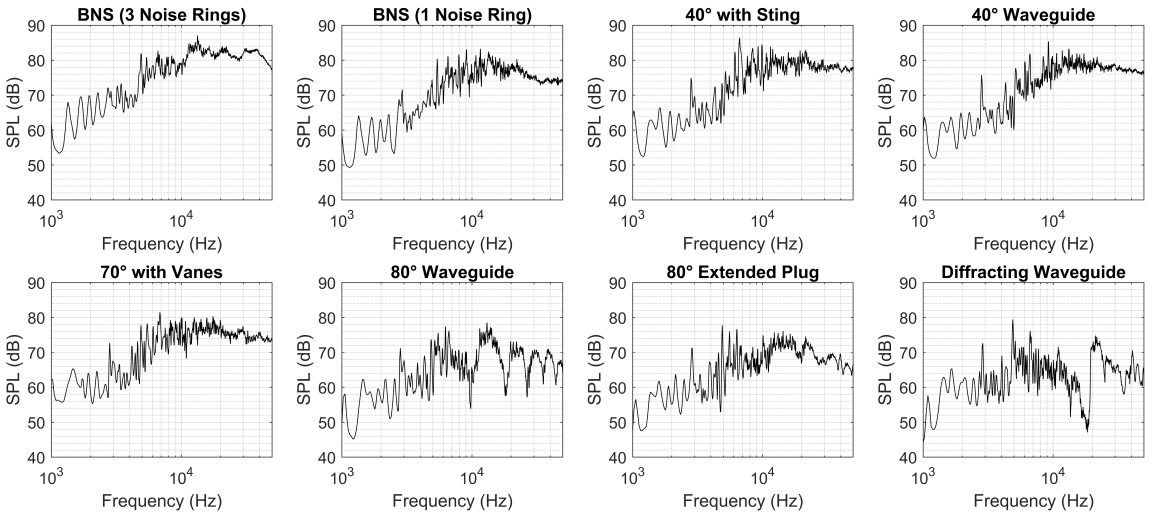

Fig. 13 Narrowband far-field acoustic spectra of the baseline BNS and all waveguide configurations at 70 psi for the 0° microphone position (in line with the exhaust axis).

A comparison of directivity and peak sound levels for all waveguide configurations with a single noise ring is presented in Figure 14. This plot shows one-twelfth octave SPL measurements at 20 kHz for a single arc measurement, where 0° is the overhead microphone position and 90° is sideline. Each configuration has a characteristic directivity pattern that is similar over the range of 10 kHz to 60 kHz. The Baseline BNS, 40° waveguides, and 70° waveguide with struts have similar directivity patterns, with peak sound levels at 0° polar angle and steadily decreasing sound levels as polar angle increases. These four configurations have direct propagation paths from the waveguide exit to the overhead microphones, resulting in peak sound levels about 10 dB higher than the 80° waveguides or the diffracting waveguide. Figure 14 shows results for a single arc measurement, but directivity was found to be axisymmetric around the exhaust axis with less than ±2 dB variation in one-twelfth octave sound pressure levels.

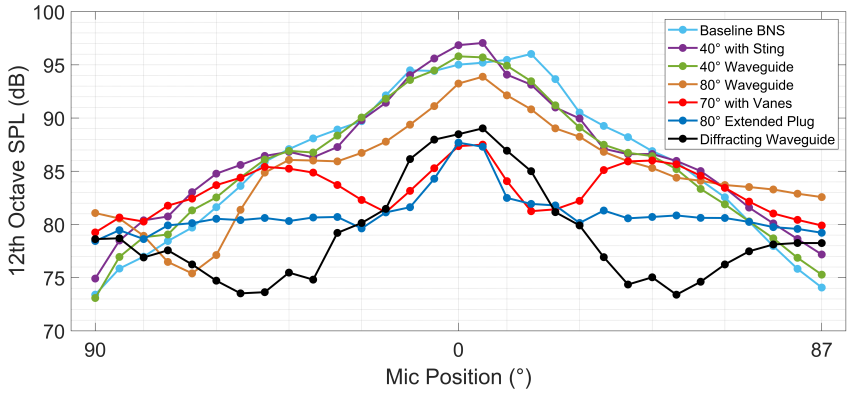

Fig. 14 Far-field directivity at 30 kHz of the baseline BNS and all waveguide configurations, where 0° aligns with the exhaust axis of the BNS and 90° is sideline.

Measurements from the isolated noise ring, original BNS, and waveguides inform the following explanation of noise propagation for the BNS. Inside the original BNS, it appears that a diffuse sound field is formed from the impinging jet noise sources radiating and reflecting off the internal surfaces of the nacelle and inlet cover. As the sound propagates towards the aft exit, it enters an annular duct formed by the nacelle aft section and plug. The diffuse field from the random source does not drive higher-order modes through the annular section, so the noise propagates primarily as a plane wave. As a result, the exit plane acts as a 'ring source' that can be thought of as a continuous, spatially coherent, distribution of point sources around the exit plane. When combined with the plug structure downstream of the exit plane, this creates a noise peak along the exit axis as illustrated in Figure 15, because all parts of the ring source can radiate to that location. This directivity, with peak noise in line with the nacelle exhaust axis, was observed for all waveguides with plugs. The waveguide configurations with more structure lowered overall radiated sound levels without changing the dominant source directivity.

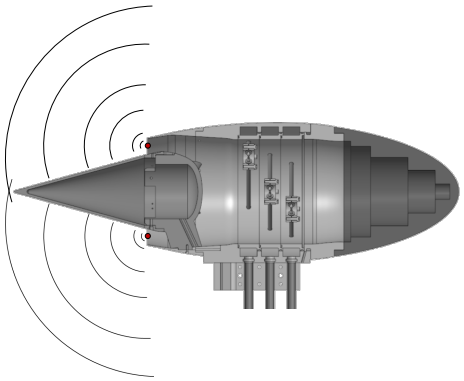

Fig. 15 Illustration of acoustic radiation to the far-field due to propagation from the ring source at the BNS outlet.

The plug attachment mechanism and presence of support struts in the plenum did not have a significant impact on the measured directivity for the 40° and 40° with sting waveguides, which show less than ±1 dB variation. The narrower channels and additional diffraction edges present in the 70° with vanes configuration did not significantly change the observed far-field directivity from the Baseline BNS case. The 70° waveguide with vanes shows a different directivity pattern, with peak sound levels at 0° and 30° polar angles. While there is still a peak at 0°, the second peak was located in the desired peak SPL location. To eliminate the direct radiation path to the 0° microphone, the diameter of the plug was extended for the 80° Extended Plug waveguide. However, this configuration still produced peak noise at 0° polar angle, with decreasing noise levels to around 20° polar angle and constant levels from 20° to 90°. The diffracting waveguide produced peak noise levels at 0° polar angle, with minimum sound levels at 50° polar angle.

Aside from the directivity characteristics discussed to this point, the desired configuration should produce high sound levels between 8 and 50 kHz. Narrowband acoustic spectra for the 0° microphone, where peak levels for all waveguide configurations (in line with the exhaust axis) are presented in Figure 13 for frequencies between 1 and 50 kHz. The BNS with three noise rings produces a spectral shape with increasing noise levels up to 10 kHz, then constant noise levels from 10-50 kHz at 83 dB ± 1 dB. The spectra for the BNS with a single noise ring and 40° waveguides produces similar spectral shapes with lower peak sound levels, approximately 78 dB. The 70° waveguide with vanes produces a similar spectral shape to the configurations discussed, but with peak noise levels around 75 dB.

Spectral peaks and dips observed for the 80° waveguide in Figure 13 suggest an interference pattern, likely caused by diffraction from the edges of the annular duct. As sound waves exit the waveguide, there are two edges - one on the converging diverging section, and one on the plug, as shown in Figure 16. The 80° waveguide provides less direct radiation of the diffuse sound field generated inside the BNS to the 0° microphone, making the diffracted sources more apparent. The interference pattern is observable for polar angles from 0° to 30°. The phase difference changes with measurement angle, resulting in the differing frequency spacing as polar angle increases, observable from 10-80 kHz in Figure 16. The 80° Extended Plug waveguide spectra suggested a slight interference pattern similar to the 80° waveguide, but the larger plug blocked more radiation to the lower polar angle microphones. The 80° Extended Plug waveguide produces increasing noise levels up to 10 kHz with a peak around 75 dB, then decreasing noise levels at higher frequencies. The interference pattern was not observed for the 70° with Vanes waveguide, but is theorized to be smeared out by the additional sharp edges present at the duct exit.

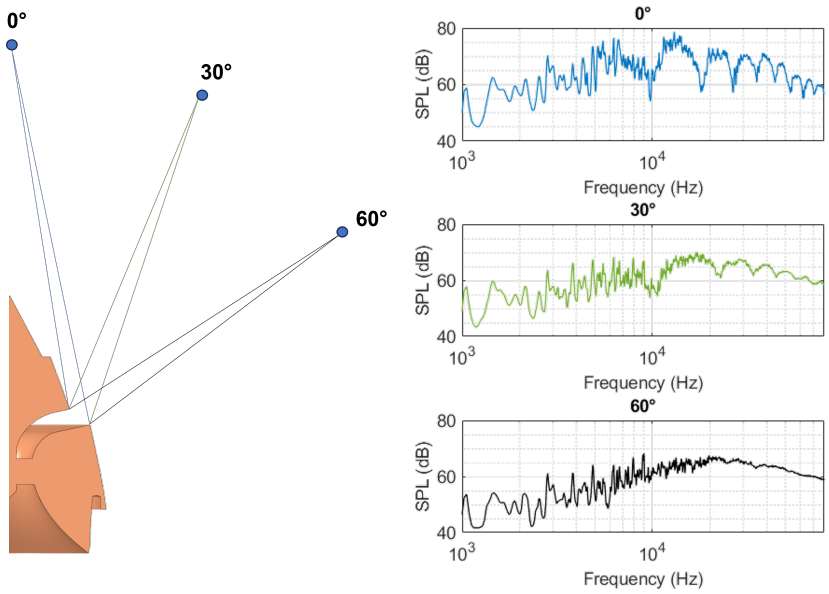

Fig. 16 Illustration of diffraction from 80° Waveguide edges and resulting phase changes observed at the narrowband spectra for the 0°, 30°, and 60° microphones.

The diffracting waveguide produced the lowest overall sound levels, as there was no direct radiation path from the impinging jets to any microphone. The desired effect of a diffracted source at the start of the duct that would propagate as a plane wave radiating towards a higher polar angle was not observed. Instead, the diffracted source, if present, was of much lower magnitude than the 'ring source', which dominated the directivity pattern. The tested waveguides produced appropriate noise levels at the frequencies of interest and had axisymmetric sound radiation, but they did not produce the desired directivity, which prompted further investigation into the isolated noise source.

C. Optimized Configurations

The ideal directivity for the simulator is based on the Kresja and Stone model, which was developed using fan noise data obtained in the NASA Glenn 9- by 15- Foot Low-Speed Wind Tunnel, and its peak directivity agrees well with other models including Heidmann [14] and Kontos [15]. At the frequencies of interest in this study (8 to 50 kHz), the isolated noise ring exhibits a directivity pattern similar to that predicted by the Kresja-Stone model for aft fan broadband noise, with peak noise levels approximately 40° off center and minimum sound levels measured by the 0° microphone. This similarity led to an exploration of various configurations aimed at preserving this directivity, plotted again as a contour for the 30 kHz frequency of interest in Figure 17 and over a single arc at 180° rotation angle for several frequencies in Figure 18. A 3D-printed plastic shell, as shown in Figure 6, was used as an inlet cover for the noise ring, intended to direct the noise radiation in a single hemisphere. This cover was filled with acoustic foam, arranged in a staggered pattern. This cover did not significantly change the overall directivity trends, as shown in Figures 17 and 18. At high microphone angles, more noise is blocked by the additional hardware, preventing a direct path between the source and the microphone.

With the acoustically treated inlet cover configuration as a prototype, the BNS was modified to attempt to match its acoustic behavior. The optimized BNS configuration, shown in Figure 7, excludes both the nacelle aft section and the plug, positioning the centered noise ring at the most downstream location, nearest to the nacelle exit. All internal surfaces of the BNS are lined with 1.5 inches of open-cell polyurethene acoustic foam to reduce scattering and ensure direct sound radiation from the jet impingement zone is dominant. With the optimized BNS, peak noise occurs near the 40° microphone, with sharper rolloff at higher microphone angles due to the presence of the duct.

To look at the spectra in the area of peak sound radiation, Figure 19 shows a comparison of the narrowband acoustic spectra of the 42° polar microphone for the baseline BNS with one noise ring, the isolated noise ring, the isolated noise

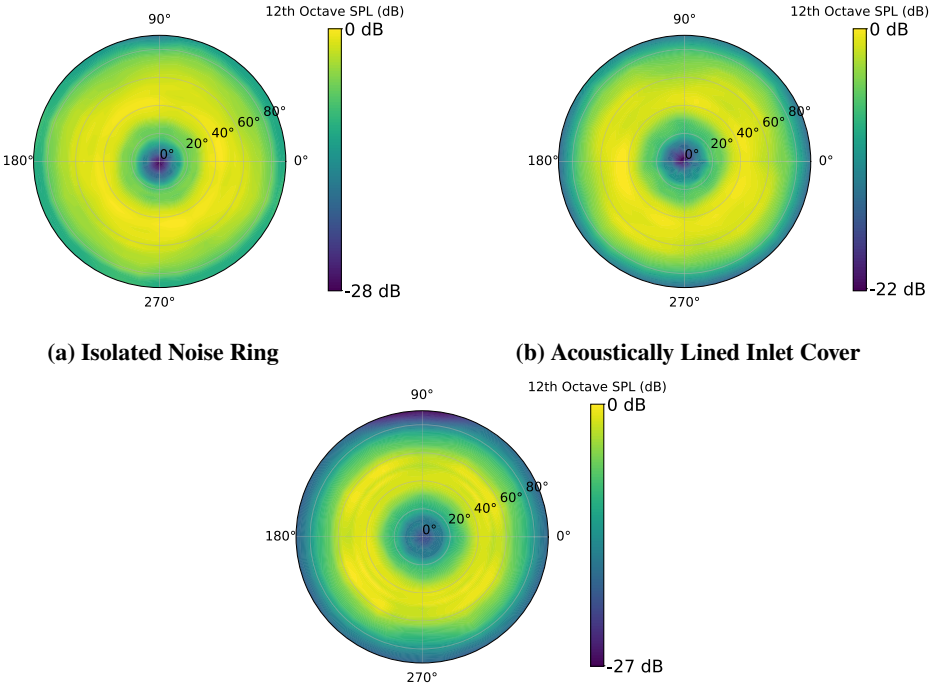

(a) Isolated Noise Ring

(b) Acoustically Lined Inlet Cover

(c) Optimized BNS

Fig. 17 30 kHz one-twelfth octave band SPL contours normalized to the contour peak level for the a) isolated noise ring, b) noise ring with acoustically lined inlet cover, and c) the optimized BNS.

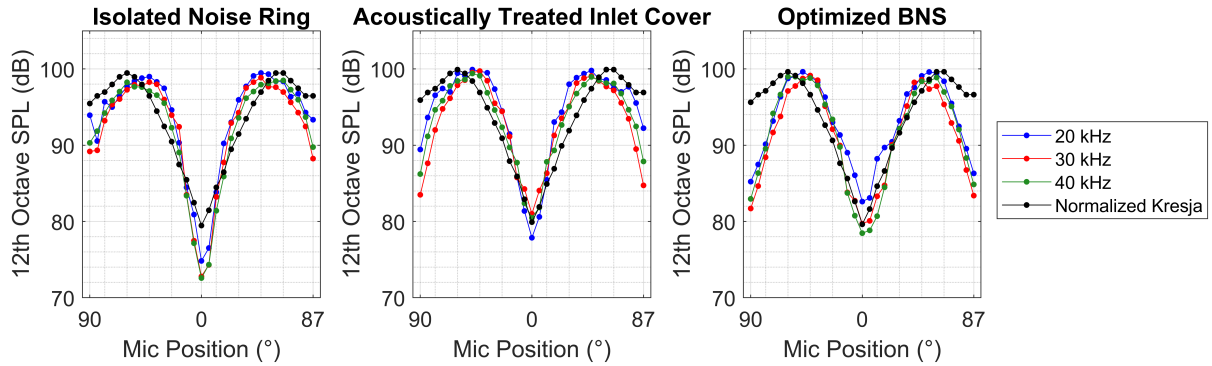

Fig. 18 Far-field directivity at 20, 30, and 40 kHz of the isolated noise ring, noise ring with acoustically lined inlet cover, and the optimized BNS.

ring with the acoustically treated inlet cover, and the optimized BNS. For all configurations shown in Figure 19, except the baseline BNS case, peak sound radiation occurs around 40° polar angle. The isolated noise ring produced similar spectra with and without the acoustically treated inlet cover, with slightly higher levels when the cover was installed. Generally, the optimized configuration of the BNS displays the best performance relative to the desired characteristics.

It was concluded that the waveguide concept could not meet the desired objective since, despite modifying the propagation through the duct, the ring source would dominate the far-field directivity. Instead, by removing the plug to open the exit plane and placing the impinging jet source near the nacelle exit, the original directivity of the isolated impinging jet fixture is largely preserved by enabling the sound to propagate freely, albeit with some constraint at higher polar angles due to the nacelle walls forming a short cylindrical duct. For future tests where aft-broadband fan noise is generated, the configuration used will depend on the requirements of the test. If sharper decrease in sound levels at

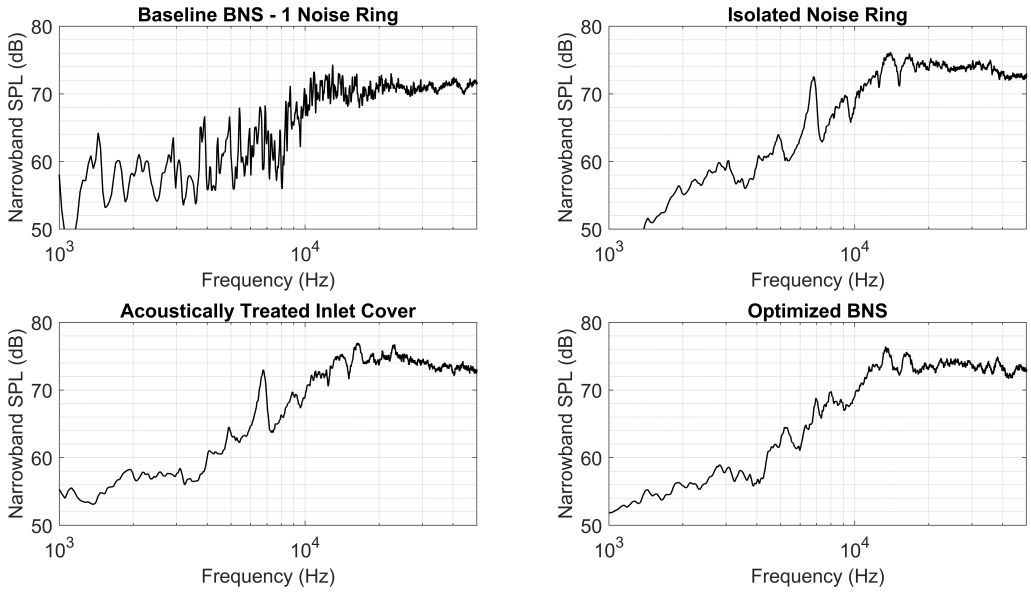

Fig. 19 Narrowband acoustic spectra of the baseline BNS with one noise ring, isolated noise ring, noise ring with acoustically lined inlet cover, and the optimized BNS for the 42° microphone position (peak noise radiation location).

sideline locations is acceptable, then the Optimized BNS configuration is preferred due to its geometric similarity to an actual engine. If sideline levels are more important, the Acoustically Treated Inlet Cover could be modified to increase geometric similarity to a turbofan engine, while preserving the higher sideline noise levels.

IV. Conclusion

This study aimed to modify an existing broadband noise simulator to better replicate the aft fan broadband noise of a ducted turbofan engine. A successful simulator would maintain geometric similarity to a real aircraft engine, generate high sound levels at frequencies between 8 and 50 kHz, and exhibit axial symmetry around the exhaust axis. The desired noise directivity for aft fan broadband noise was based on the Kresja-Stone model [5] with peak sound levels approximately 40° from the exhaust axis. Initial modifications involved 3D-printed components, referred to as waveguides, that replaced the aft nozzle and plug sections of the existing BNS model to attempt to direct sound waves towards the desired positions. Results from these configurations prompted a deeper investigation into the noise source itself, focusing on the effects of various simulator components. This investigation revealed that the BNS noise source was not behaving as previously assumed, and the focus of the modifications shifted from changing the BNS directivity to preserving the directivity of the impinging jet source itself. Successful configurations were identified that met the desired characteristics of the simulator. These results support the goal of creating a versatile noise source for future experiments investigating the scattering effects of individual engine noise components interacting with airframe structures.

By investigating a wide parameter space and analyzing the individual components, this study enhanced the understanding of noise-generating mechanisms of the impinging jets within the simulator. The findings provide a physical explanation for the observed noise characteristics, which align with previous computational studies [8], and will guide future designs to achieve more precise control over the noise source in subsequent experiments. The modified simulator will be integrated with airframe models to further study propulsion airframe aeroacoustic effects, playing a crucial role in the development of advanced noise mitigation strategies, especially for unconventional aircraft designs.

References

[1] Basner, M., Clark, C., Hansell, A., Hileman, J., Janssen, S., Shepherd, K., and Sparrow, V., "Aviation Noise Impacts: State of the Science," *Noise and Health*, Vol. 19(87), 2017, pp. 41–50. https://doi.org/10.4103/nah.NAH_104_16, URL https://journals.lww.com/nohe/fulltext/2017/19870/aviation_noise_impacts__state_of_the_science.1.aspx.

[2] June, J., Thomas, R. H., and Guo, Y., "System Noise Technology Roadmaps for a Transonic Truss-Braced Wing and Peer Conventional Configuration," *28th AIAA/CEAS Aeroacoustics 2022 Conference*, American Institute of Aeronautics and Astronautics, Southampton, UK, 2022. https://doi.org/10.2514/6.2022-3049.

[3] Clark, I., Thomas, R. H., and Guo, Y., "Aircraft System Noise Assessment of the NASA D8 Subsonic Transport Concept," *2018 AIAA/CEAS Aeroacoustics Conference*, American Institute of Aeronautics and Astronautics, Atlanta, GA, 2018. https://doi.org/10.2514/6.2018-3124.

[4] Thomas, R. H., Burley, C. L., and Nickol, C. L., "Assessment of the Noise Reduction Potential of Advanced Subsonic Transport Concepts for NASA's Environmentally Responsible Aviation Project," *54th AIAA Aerospace Sciences Meeting*, American Institute of Aeronautics and Astronautics, San Diego, California, 2016. https://doi.org/10.2514/6.2016-0863.

[5] Krejsa, E. A., and Stone, J. R., "Enhanced Fan Noise Modeling for Turbofan Engines," NASA CR 2014-218421, Dec. 2014. URL https://ntrs.nasa.gov/citations/20150000884.

[6] Clark, I., Nesbitt, E., Thomas, R. H., and Guo, Y., "Turbofan Aft-Radiated Broadband Acoustic Flight Effects," *30th AIAA/CEAS Aeroacoustics Conference (2024)*, American Institute of Aeronautics and Astronautics, Rome, IT, 2024. https://doi.org/10.2514/6.2024-3225.

[7] Hutcheson, F. V., Brooks, T. F., Burley, C. L., Bahr, C. J., Stead, D. J., and Pope, D. S., "Shielding of Turbomachinery Broadband Noise from a Hybrid wing Body Aircraft Configuration," *20th AIAA/CEAS Aeroacoustics Conference*, American Institute of Aeronautics and Astronautics, Atlanta, GA, 2014. https://doi.org/10.2514/6.2014-2624.

[8] Brehm, C., Housman, J. A., Kiris, C. C., and Hutcheson, F. V., "Noise Characteristics of a Four-Jet Impingement Device Inside a Broadband Engine Noise Simulator," *21st AIAA/CEAS Aeroacoustics Conference*, American Institute of Aeronautics and Astronautics, Dallas, TX, 2015. https://doi.org/10.2514/6.2015-2211.

[9] Rizzi, S., Cabell, R., and Allen, A., "Recent enhancements to the NASA Langley Structural Acoustics Loads and Transmission (SALT) facility," *International Conference on Recent Advances in Structural Dynamics*, 2013. URL https://ntrs.nasa.gov/citations/20140000590.

[10] Shelts, K., Galles, M., and Zawodny, N., "Acoustic Characterization of the High Resolution Traversing Microphone Array," *Future TM*, 2025.

[11] Czech, M. J., Thomas, R. H., and Elkoby, R., "Propulsion Airframe Aeroacoustic Integration Effects for a Hybrid Wing Body Aircraft Configuration," *International Journal of Aeroacoustics*, Vol. 11, No. 3-4, 2012, pp. 335–368. https://doi.org/https://doi.org/10.1260/1475-472X.11.3-4.335.

[12] Gerhold, C. H., Clark, L. R., Dunn, M. H., and Tweed, J., "Investigation of acoustical shielding by a wedge-shaped airframe," *Journal of Sound and Vibration*, Vol. 294, No. 1-2, 2006, pp. 49–63. https://doi.org/10.1016/j.jsv.2005.10.010.

[13] Clark, L., and Gerhold, C., "Inlet Noise Reduction by Shielding for the Blended-Wing-Body Airplane," *5th AIAA/CEAS Aeroacoustics Conference and Exhibit*, American Institute of Aeronautics and Astronautics, Bellevue, WA, 1999. https://doi.org/10.2514/6.1999-1937.

[14] Heidmann, M. F., "Interim Prediction Method for Fan and Compressor Source Noise," NASA TM X-71763, Jun. 1975. URL https://ntrs.nasa.gov/citations/19750017876.

[15] Kontos, K. B., Janardan, B. A., and Gliebe, P. R., "Improved NASA-ANOPP Noise Prediction Computer Code for Advanced Subsonic Propulsion Systems," NASA CR 195480, Aug. 1996. URL https://ntrs.nasa.gov/citations/19960048499.